Cohesiveness tunes assembly and morphology of FG nucleoporin domain meshworks – Implications for nuclear pore permeability

*Nico B. Eisele, Aksana A. Labokha, Steffen Frey, Dirk Görlich, Ralf P. Richter**

corresponding author: rrichter@cicbiomagune.es

Cohesiveness tunes assembly and morphology of FG nucleoporin domain meshworks – Implications for nuclear pore permeability

Nico B. Eisele[†‡], *Aksana A. Labokha*[‡], *Steffen Frey*[‡], *Dirk Görlich*[‡], *Ralf P. Richter*[†§¶*]

[†] Biosurfaces Unit, CIC biomaGUNE, Paseo Miramon 182, 20009 San Sebastian, Spain

[‡] Department of Cellular Logistics, Max Planck Institute for Biophysical Chemistry, Am Faßberg 11, 37077 Göttingen, Germany

[§] I2BM, Department of Molecular Chemistry, J. Fourier University, 570 Rue de la Chimie, 38041 Grenoble Cedex 9, France

[¶] Max Planck Institute for Intelligent Systems, Heisenbergstraße 3, 70569 Stuttgart, Germany

* Correspondence: rrichter@cicbiomagune.es

Running title. Cohesiveness tunes FG domain meshworks

Keywords. brush; gel; nuclear pore complex; permeability barrier; nucleo-cytoplasmic transport; supramolecular self-organization

Abstract. Nuclear pore complexes control the exchange of macromolecules between the cytoplasm and the nucleus. A selective permeability barrier which arises from a supramolecular assembly of intrinsically unfolded nucleoporin domains rich in phenylalanine-glycine dipeptides (FG domains) fills the nuclear pore. There is increasing evidence that selective transport requires cohesive FG domain interactions. To understand the functional roles of cohesive interactions, we studied monolayers of end-grafted FG domains as a bottom up nanoscale model system of the permeability barrier. Based on detailed physico-chemical analysis of the model films and comparison of the data with polymer theory, we propose that cohesiveness is tuned to promote rapid assembly of the permeability barrier and to generate a stable and compact pore-filling meshwork with a small mesh size. Our results highlight the functional importance of weak interactions, typically a few k_BT per chain, and contribute important information to understand the mechanism of size-selective transport.

INTRODUCTION

Bulk macromolecular transport between the cytosol and the nucleus of eukaryotic cells is gated through nuclear pore complexes (NPCs) (1,2,3,4,5,6), large protein assemblies that perforate the nuclear envelope. To form an NPC, several types of nucleoporin proteins self-assemble in multiple copies into a ring-like structure with a central channel of 30 to 50 nm in diameter (7,8). Specialized nucleoporin domains that are natively unfolded and rich in FG dipeptides (FG domains) are grafted at high density to the channel walls (9) and constitute a selective permeability barrier: molecules smaller than 5 nm in diameter (10) can diffuse efficiently through the channel, whereas larger molecules are delayed or blocked, unless they are bound to nuclear transport receptors (NTRs) which bind to FG motifs as a prerequisite for facilitated NPC passage (1,2,3,4,11).

The physical mechanism behind transport selectivity is poorly understood. Several models have been proposed (12,13,14,15,16). They share the idea that the permeability barrier of NPCs arises from the supramolecular assembly of FG domains. The structure of the FG domain meshwork inside the NPC remains elusive, presumably because it is highly dynamic and exhibits a low degree of order. There is, however, increasing evidence that FG domains can interact attractively with each other (17,18,19,20), and that these interactions are essential for the formation of a functional permeability barrier (17,21).

We hypothesize that the combination of flexible chains, their confinement through grafting, and the degree to which they interact attractively with each other, henceforward also called cohesiveness, determines the functionality of the permeability barrier. Cohesive interactions are heterogeneously distributed within FG domain chains, i.e. one can find cohesive elements, made of FG, FxFG, or GLFG motives but also other amino acids, as well as repulsive ones, such as stretches of charged residues (19,22,23,24,25). The balance of these interactions, together with the confinement of the chains, will ultimately determine the organization and dynamics of the nanoscale FG domain meshwork in a way that is crucially important for function, yet, not well understood.

To explore experimentally how the balance of interactions affects the morphology and dynamics of FG domain assemblies, we exploited a recently developed nanoscale model system of the permeability barrier: planar films of FG domains that are end-grafted to supported lipid bilayers (SLBs) (Fig. 1 *a*) (26,27). The films reproduce the native permeability barrier in the following aspects: the FG domains are end-grafted, the film thickness is comparable to the dimensions of the nuclear pore, and the FG repeat densities are comparable. Compared to the native pore or reconstituted systems that reproduce the pore-like topology (21,28), the choice of a planar geometry provides excellent control on film formation and greatly facilitates a detailed and quantitative characterization of the film morphology and dynamics.

To rationalize the behavior of our films, we took advantage of classical theoretical concepts of polymer physics. As a first approximation, we describe the physico-chemical ensemble properties of FG domain assemblies by their average degree of cohesive interactions, without considering the (still unknown) exact distribution of cohesive elements along the chain. Fig. 1 *b* schematically shows theoretical predictions about the morphology of end-grafted and flexible, regular polymers of varying cohesiveness (29,30). For regular polymers, cohesiveness receives a precise physical meaning. It is identical to the so-called Flory interaction parameter χ, which is determined by the relative strength of (inter- and intra-molecular) interactions between polymer segments, polymer-solvent and solvent-solvent interactions. Irrespective of the magnitude of χ, a sufficiently high grafting density entails the formation of a so-called brush, in which the film is

laterally homogeneous and its chains are partially stretched away from the grafting surface. With increasing χ, the stretching decreases and an increasingly dense film is expected to form. For values of χ well beyond 0.5, lateral phase separation occurs at intermediate grafting densities, driven by the maximization of inter-chain interactions. Depending on the grafting density and χ, different morphologies can arise (30,31): a continuous film perforated by pores, an array of isolated clusters of several polymer chains, or an array of globules of individual chains. Flexible chains in a brush do also explore the lateral dimensions, implying that they show some degree of interpenetration. This aspect is frequently neglected when sketching polymer brushes (e.g. in refs. (16) and (32)) yet it might be functionally important. On a local scale, the film forms a meshwork of interpenetrating chains, and the so-called correlation length ξ is a measure for the mean mesh size (33,34,35). The mesh size limits the permeability of particles that do not attractively interact with the polymers (34).

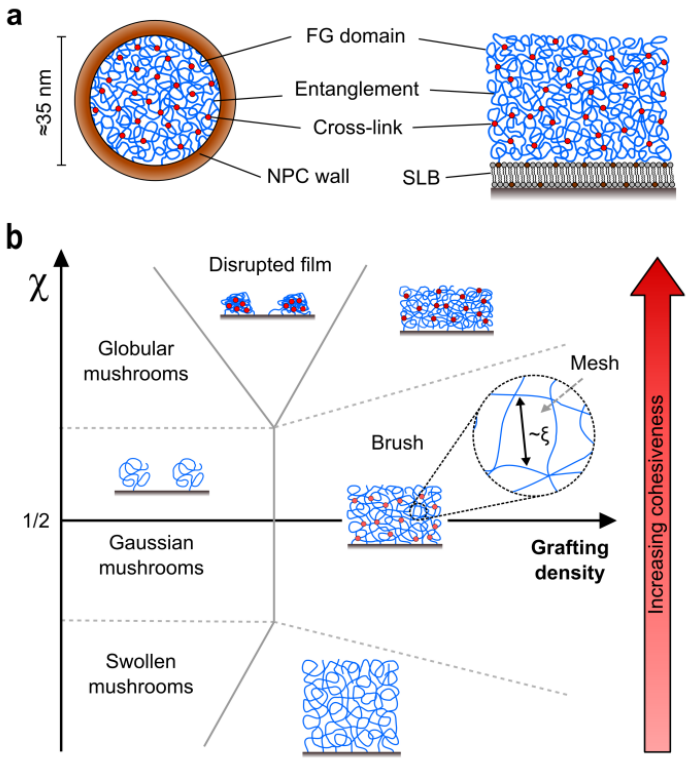

FIGURE 1: Supramolecular assembly of FG domains, and predictions by polymer theory. (*a, left*) Schematic cross section of the yeast NPC perpendicular to its axis. FG domains are anchored to the NPC wall at high density. The flexible, intrinsically disordered chains explore the NPC channel, interpenetrate, and may form cross-links (*red circles*) to form the permeability barrier. (*a, right*) Monolayers of SLB-grafted FG domains are used as model systems of the permeability barrier, to study the impact of cohesive interactions on the organization and dynamics of FG domain assemblies at the nm scale. (*b*) Schematic phase diagram, summarizing simple theoretical predictions for films of flexible, regular, end-grafted polymers as a function of the Flory interaction parameter χ (which, as we propose, mirrors overall cohesiveness in our irregular FG domains) and grafting density. The brush and disrupted film phases are of particular interest for this study. Boundaries between phases are drawn qualitatively. The interpenetration of chains in the brush film (*inset*) gives rise to the correlation length ξ, a measure of the average mesh size.

In this paper, we provide evidence that FG domains, despite their heterogeneous primary structure, faithfully reproduce the basic theoretical predictions for regular, flexible polymers. To this end, we compared different types of FG domains, including mutants. The FG domains were selected for their difference in cohesiveness, based on their propensity to form macroscopic hydrogels, where a hydrogel is defined as a non-fluid polymer network that is expanded throughout its whole volume by aqueous solvent (36). "Nup98-glyco" is an O-GlcNAc-modified, 485 amino acid long FG domain from *Xenopus tropicalis* Nup98. This domain forms tight macroscopic hydrogels and is essential for forming a selective permeability barrier in NPCs reconstituted from *Xenopus* egg extracts (21,25). Nsp1-WT, a 600 amino acid FG domain from *Saccharomyces cerevisiae*, consists of a highly cohesive N-terminal domain and a less cohesive C-terminal domain (19,32) but still forms tight macroscopic hydrogels (17,18). Nsp1-FILV→S, a mutant Nsp1 FG domain in which all hydrophobic amino acids were exchanged by the hydrophilic serine, does not form macroscopic hydrogels (19).

In particular, we analyze to what extent ultrathin films of the selected FG domain constructs form hydrogels. In the nucleocytoplasmic transport field, the scenario of end-grafted, non-cohesive chains is commonly, though imprecisely, termed a "brush-like, entropic barrier" and opposed to a gel (16,37). Based on the above-given definitions, it becomes clear that polymer brushes and hydrogels are not mutually exclusive states: the chains in a polymer brush (i.e. a dense arrangement of end-grafted polymer chains) may repel each other, leading to simple interpenetration of chains, or attract each other at various degrees, leading to the formation of a (transiently or stably) cross-linked film; if the cross-links are stable enough to prevent polymer flow, a hydrogel would be formed.

We demonstrate that the morphologies outlined in Fig. 1 *b* can be generated if the cohesiveness is adjusted appropriately. We will see that hydrogels on the one hand and brushes of interpenetrating, non-cohesive chains on the other are not two distinct states but that they are extremes of a continuous spectrum of states that can be covered by tuning cohesiveness. We argue that the self-organization phenomena that we observe on planar surfaces are relevant for the NPC topology, and discuss the broad implications for the assembly and function of the permeability barrier.

MATERIALS AND METHODS

Proteins and buffer

We used the following FG domains: Nsp1-WT (amino acids 2 to 601; 62.1 kDa), Nsp1-F→S (58.8 kDa), Nsp1-FILV→S (57.9 kDa), and Nup98-glyco (amino acids 1 to 485, with about 30 O-GlcNAc modified Ser and Thre residues per chain (25); 55.3 kDa) without His-tag; Nsp1-WT (64.1 kDa), Nsp1-F→S (60.8 kDa), and Nsp1-FILV→S (60.4 kDa) with C-terminal His_{10}-tag; and Nup98-glyco (58.8 kDa) with N-terminal His_{14}-tag. FG domains with and without a His-tag were purified as described earlier (25,26) (Fig. S1 in the Supporting Material). To obtain fluorescently labeled FG domains, the N-terminal cysteine of the Nsp1 FG domain constructs and the C-terminal cysteine of Nup98-glyco were reacted with Atto488-maleimide and purified by high-performance liquid chromatography as described previously (18). All FG domains were stored at a concentration of 10 mg/ml in 50 mM Tris pH 8 and 6 M guanidine hydrochloride (GuHCl) at -80ºC. Prior to use, the FG domains were diluted in working buffer (10 mM Hepes, pH 7.4, 150 mM NaCl) to desired concentrations. The dilutions were chosen such that the residual concentration of GuHCl in the final solution was below 75 mM.

Surfaces

Silica-coated QCM-D sensors (QSX303, Biolin Scientific, Västra Frölunda, Sweden) and silicon wafers with a native oxide layer of less than 2 nm thickness (University Wafers, South Boston, MA, USA) were cleaned by immersion in a 2 % sodium dodecyl sulfate solution for 30 min, rinsing with ultrapure water, blow-drying with nitrogen, and exposure to UV/ozone (BioForce Nanosciences, Ames, IA, USA) for 30 min. Glass cover slips (#1.5, 24×24 mm^2; Menzel Gläser, Thermo Scientific, Germany) were immersed in freshly prepared piranha solution, i.e. a 1:3 (*v*/*v*) mixture of 50 % H_2O_2 and concentrated H_2SO_4 for 1 h, rinsed with ultrapure water, and blow-dried with nitrogen. Cleaned substrates were stored in air and again exposed to UV/ozone (30 min) prior to use.

Preparation of lipids and lipid vesicles

Lyophilized dioleoylphosphatidylcholine (DOPC) was purchased from Avanti Polar Lipids (Alabaster, AL, USA). Lipid analogues with chelator headgroups comprising either two or three nitrilotriacetic acid moeieties (bis-NTA or tris-NTA, respectively (38)) were kindly provided by J. Piehler (University of Osnabrück, Germany). Lipid vesicles were prepared as described earlier (38,39). Before use, vesicle suspensions were diluted to 50 μg/ml in working buffer containing 10 mM $NiCl_2$.

Quartz crystal microbalance with dissipation monitoring (QCM-D)

QCM-D measures changes in resonance frequency, Δf, and dissipation, ΔD, of a sensor crystal upon interaction of (soft) matter with its surface. The QCM-D response is sensitive to the mass (including hydrodynamically coupled water) and the mechanical properties of the surface-bound layer (40). To a first approximation, a decrease in Δf indicates a mass increase, while high (low) values of ΔD indicate a soft (rigid) film. Adsorption processes were monitored *in situ* with sub-second time resolution. QCM-D measurements were performed with a Q-Sense E4 system (Biolin Scientific). The system was operated in flow mode with a flow rate of typically 20 μl/min using a syringe pump (KD Scientific, Holliston, MA, USA). The working temperature was 23°C. Δf and ΔD were measured at the fundamental ($i = 1$) and typically 6 overtones ($i = 3, 5 \ldots 13$), corresponding to resonance frequencies of $f_i \approx 5, 15, 25 \ldots 65$ MHz. Changes in dissipation and normalized frequencies, $\Delta f_i/i$, for $i = 5$ are presented. The film thickness h_{QCM} was determined by fitting of QCM-D data to a viscoelastic model, as described in ref. (27).

Spectroscopic ellipsometry (SE)

SE (M2000V, Woollam, NE, USA) on silicon wafers was performed using an open fluid cell with continuously stirred sample solution, and data were fitted with the software CompleteEASE (Woollam, NE, USA) using a model of multiple optically homogeneous layers, as previously described (26,41). The FG domain film was treated as a transparent Cauchy medium with optical thickness h_{SE} and wavelength-dependent refractive index n. The FG domain grafting density was determined through de Fejter's equation (42), $\Gamma = h_{SE}\Delta n/\left(M_w \times \mathrm{d}n/\mathrm{d}c\right)$, where M_w is the molecular weight, and Δn the (approximately wavelength-independent) difference in refractive index between film and buffer solution. We used a refractive index increment of $\mathrm{d}n/\mathrm{d}c = 0.18$ cm^3/g. Error bars for h_{SE} in Fig. 3 *b* correspond to 68% confidence intervals, calculated analogously to the error bars for $h_{QCM\text{-}D}$, see ref. (27) for details.

Atomic force microscopy (AFM)

Imaging and nanoindentation measurements were performed on a NanoWizard II AFM (JPK, Berlin, Germany) using oxide-sharpened Si_3N_4 probes (NP-S, Veeco, CA, USA) with a nominal

cantilever spring constant of 0.06 N/m. The real spring constant, determined through the thermal noise method, was 0.10 N/m. Sample films were prepared on silicon wafers, following the same incubation steps as previously established by SE (Figs. 2 and S3), although in still solution. Complementary SE measurements confirmed that stirring does not significantly affect the final adsorbed amounts for the incubation times used (1 h or more).

AFM images were acquired in tapping mode in solution. The drive frequency was typically between 10 and 20 kHz, and the free amplitude of the cantilever was set to about 30 nm. To ensure a soft approach to the sample, the setpoint amplitude was decreased manually, in steps of a few Å, until the surface could be tracked. Scan speeds of 2 to 20 μm/s were employed.

Nanoindentation assays were performed in working buffer solution. Deflection vs. displacement curves were typically acquired at approach speeds of 500 nm/s and maximal loads of 1 nN, and converted into force vs. distance curves with JPK Data Processing software. We compared only force curves that were acquired with the same tip, in order to minimize the effect that variations in the shape of the AFM probe may have on indentation. Reference force curves were acquired on a control surface – an SLB that lacked FG domain coating – before and after indentation of each FG domain film. Only indentation series which reproducibly showed a small interaction distance (≤5 nm) on bare SLBs were accepted. A force curve was considered representative, when it could be reproduced upon repeated indentation at the same spot and at different spots on the same sample. For further analysis, and display in Fig. 3 *a*, 6 to 12 curves were taken with the same AFM probe on the same or different spots on a given FG domain film and averaged. To quantify the onset of repulsive forces, data around the estimated contact point were fitted with a polynomial; the onset was then taken as the distance at which the force exceeded baseline level by 10 pN. The film thickness h_{AFM} was estimated from the distance between the onset of repulsive forces and the hard-wall compression limit.

Fluorescence recovery after photobleaching (FRAP)

FRAP measurements were performed with a confocal laser scanning microscope (LSM 510, Zeiss, Germany) using an argon laser (λ = 488 nm), a plan-apochromat 63×/1.4 oil immersion objective and a completely opened pinhole (1 mm diameter). FG domain films were assembled on glass cover slips, from protein solutions containing approximately 1 mol-% Atto488-labeled FG domains. The image size was set to $118 \times 118\ \mu m^2$. After acquiring several pre-bleach images of the fluorescently labeled FG domain monolayer, a circular region with a radius of 10 μm in the center of the imaged area was bleached through brief exposure (3 to 8 s) to high laser intensity. More than 60 % bleaching in the center of the exposed region was achieved. Fluorescence recovery due to lateral diffusion of bleached (unbleached) FG domains out of (into) the bleached region was then monitored through acquisition of post-bleach images over a period of up to 4 h.

RESULTS

FG domain film assembly and its kinetics

Specific and stable end-grafting of FG domains with different cohesiveness (Nup98-glyco, Nsp1-WT, and Nsp1-FILV→S) through terminal His-tags to SLBs doped with Ni^{2+}-NTA functionalized lipids (38) was confirmed by quartz crystal microbalance with dissipation monitoring (QCM-D; Figs. S2-3). Grafting density and film formation kinetics were quantified by spectroscopic ellipsometry (SE; Fig. 2 *a*). The different FG domains initially adsorbed with similar rates, consistent with mass-transport-limited binding. Clearly, all FG domains can bind

rapidly to a sparsely covered SLB, i.e. binding of the His-tag to the Ni^{2+}-NTA group is not rate limiting. The adsorption rates decreased with increasing surface density, and the decrease in rate differed drastically between FG domains: it was very pronounced for Nsp1-FILV→S, less pronounced for Nsp1-WT, and barely noticeable for Nup98-glyco up to $\Gamma = 10$ pmol/cm^2. The grafting densities of both Nsp1 constructs remained well below this density during the first hour of incubation, indicating that availability of Ni^{2+}-NTA anchor groups did not limit binding of Nsp1 constructs within this time.

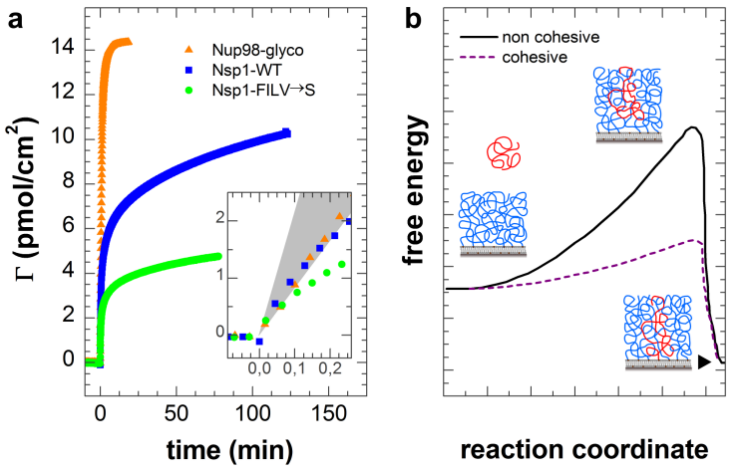

FIGURE 2: Kinetics of FG domain film assembly and maximal grafting density depend strongly on FG domain type. (*a*) Film formation was monitored by ellipsometry. At 0 min, 0.9 μM FG domains were added to SLBs containing 10 mol-% bis-NTA functionalized lipids. All FG domains were incubated under identical stirring conditions. Initial adsorption (*inset*) is similar for all FG domains and limited by mass transport (the *gray shaded area* represents theoretically estimated mass transport rates, see Supporting Material for details). At higher coverage, adsorption rates differ significantly between FG domains. (*b*) Schematic free energy profiles for the binding of FG domain molecules to an FG-domain-covered SLB. The barrier due to entropically unfavorable partitioning of new molecules into the existing FG domain film (*black curve*) is lowered through weak, attractive inter-chain interactions (*purple curve*).

A strongly coverage-dependent decrease in the binding rate, as observed for the Nsp1-FILV→S mutant, is consistent with theoretical predictions for the formation of brushes from polymer chains that repel each other ($\chi < 0.5$): the brush-forming polymers constitute an entropic barrier (Fig. 2 *b*) against the access of free polymers from solution to the SLB, entailing a coverage-dependent reduction in the binding rate (43). Cohesive interactions would be predicted to facilitate entry and partitioning of polymers into the surface-confined film, and we propose that this is the reason why Nsp1-WT and Nup98-glyco continue to bind rapidly at surface coverages that are inhibitory for Nsp1-FILV→S. The entropic penalty associated with the partitioning of polymers from the solution into the film increases with coverage, and differences in the cohesiveness would readily explain why Nup98-glyco retained a high binding rate longer than Nsp1-WT.

Thickness, concentration, and mechanical properties of FG domain meshworks

To test how cohesive interactions affect FG domain film thickness, we prepared and compared different FG domain films at grafting densities close to the maximal coverage attainable with

Nsp1-FILV→S (i. e. 5.1 ± 0.3 pmol/cm^2, or one molecule per 31 ± 2 nm^2; Fig. S4). These values compare well with the estimated average surface area per FG domain chain in a yeast NPC which would be 24 - 32 nm^2, assuming a channel of 35 - 40 nm in diameter and 30 - 35 nm in length (7), and approximately 136 FG domains per channel (9,44).

AFM indentation assays with a nanosized probe (Fig. 3) revealed film thicknesses in the range of a few 10 nm, consistent with the formation of a monolayer of weakly extended polypeptide chains. The Nsp1-FILV→S mutant formed the thickest films (35 ± 5 nm), Nsp1-WT a film of intermediate thickness (25 ± 8 nm), and Nup98-glyco the thinnest film (17 ± 3 nm). Thickness values determined from QCM-D and SE data of films prepared under identical conditions showed the same trend (Fig. 3 *b*), corroborating the AFM data. From the thickness determined by AFM and the grafting density, we can estimate the concentration of FG domains in the films to be 85 ± 13 mg/ml for Nsp1-FILV→S, 146 ± 47 mg/ml for Nsp1-WT, and 191 ± 34 mg/ml for Nup98-glyco. Clearly, increasing cohesive interactions promotes the formation of more compact films with higher FG domain concentration.

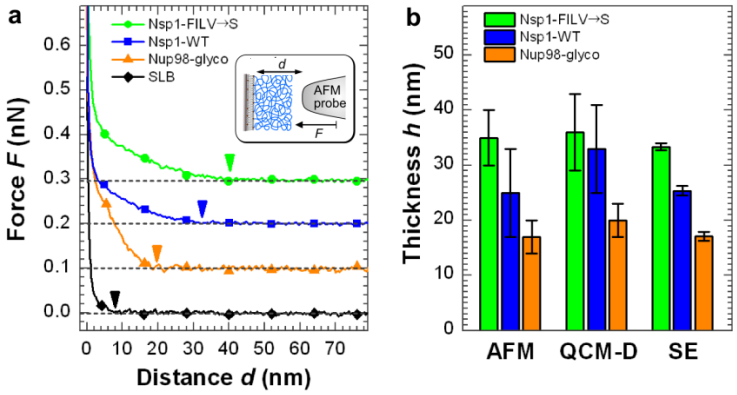

FIGURE 3: The strength of inter-FG repeat interactions affects the thickness and concentration of FG domain films. (*a*) AFM indentation assays (schematically described in the inset) on FG domain films with a grafting density of 5.4, 5.1, and 4.8 pmol/cm^2 for Nup98-glyco, Nsp1-WT, and Nsp1-FILV→S, respectively, were carried out to estimate the film thickness. The thickness was determined by the distance between the onset of repulsive forces (*arrowheads*) and the hard-wall compression limit (d = 0). Control curves on SLB-covered silica before and after the indentation assays were taken to validate that the interaction with the probe remained short-ranged. (*b*) Film thicknesses determined by AFM indentations assays, and independently through viscoelastic modeling of QCM-D data (Fig. S5) and optical modeling of ellipsometry data on identically prepared FG domain films. The stronger the cohesive interactions the thinner and denser the film.

A polymer meshwork should become stiffer when increasing the concentration or interaction strength. For thin, homogeneous films, the elastic compliance (or inverse of stiffness), J', can be estimated directly from QCM-D data (27,45). Fig. 4 displays the evolution of the ratio of QCM-D dissipation and frequency shifts, $\Delta D/-\Delta f$, which is proportional to J'/ρ, where ρ is the film density, during the process of film formation. All curves exhibited a monotonous decrease in $\Delta D/-\Delta f$ with increasing absolute frequency shifts (or surface coverage), consistent with a gradual increase in protein concentration and perhaps even attractive interactions within the films (27). The magnitudes of the $\Delta D/-\Delta f$ values varied significantly between FG domain types,

indicating that film stiffness indeed depends on the quality of the respective FG domain. Nup98-glyco and Nsp1-FILV→S formed the most rigid and soft films, respectively, while Nsp1-WT formed films of intermediate rigidity, consistent with the trends observed for film compaction and film formation kinetics. Interestingly, we could not find any difference in stiffness between Nsp1-FILV→S and another Nsp1 construct in which exclusively phenylalanines were mutated to serines (Nsp1-F→S). This indicates that F is essential for formation of the cross-links that make Nsp1-WT stiffer than its mutant forms, whereas I, L and V, which together contribute only 19% of the total content in hydrophobic amino acids of the Nsp1 FG domain, only play a subordinate role.

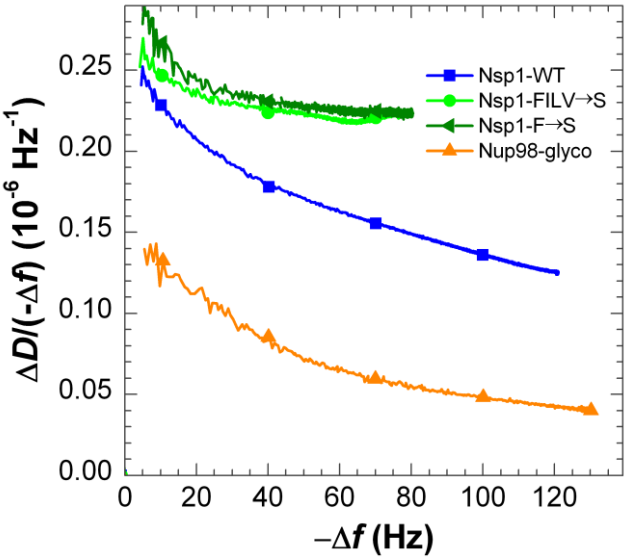

FIGURE 4: Cohesive interactions lead to stiffer FG domain films. A parametric plot of $\Delta D/-\Delta f$ vs. $-\Delta f$, monitored by QCM-D during film formation, provides an estimate of the evolution of the elastic compliance (inverse of stiffness) of FG domain monolayers with coverage. Differences in the mechanical properties of the FG domain films can be clearly discriminated by this plot. To evaluate the contribution of phenylalanines to the stiffness of Nsp1-WT meshworks, we included additionally an Nsp1 construct in which exclusively phenylalanines were mutated to serines (Nsp1-F→S). Nsp1-F→S and Nsp1-FILV→S exhibited very similar curves, indicating that the F→S mutation is sufficient for the loss of cohesive interactions compared to Nsp1-WT.

Lateral homogeneity of and chain mobility in FG domain meshworks

To test how the nature of the FG domains affects the supramolecular organization along the surface plane, we imaged FG domain films at selected grafting densities by AFM (Fig. 5). Nup98-glyco films at grafting densities of 12 and 9 pmol/cm^2 (Fig. 5 *a*-*b*) appeared overall homogeneous. Small-scale surface corrugations with a characteristic lateral length scale of about 20 nm could be clearly imaged, whereas any feature of smaller size eluded imaging. When decreasing the surface density to 5.4 pmol/cm^2 (Fig. 5 *c*), depressions appeared. The depressions were shallow yet their diameter of typically about 100 nm was already several times wider than the transport channel of NPCs. When further decreasing the grafting density, the film became very heterogeneous, showing holes of several 100 nm in diameter (Fig. 5 *d*).

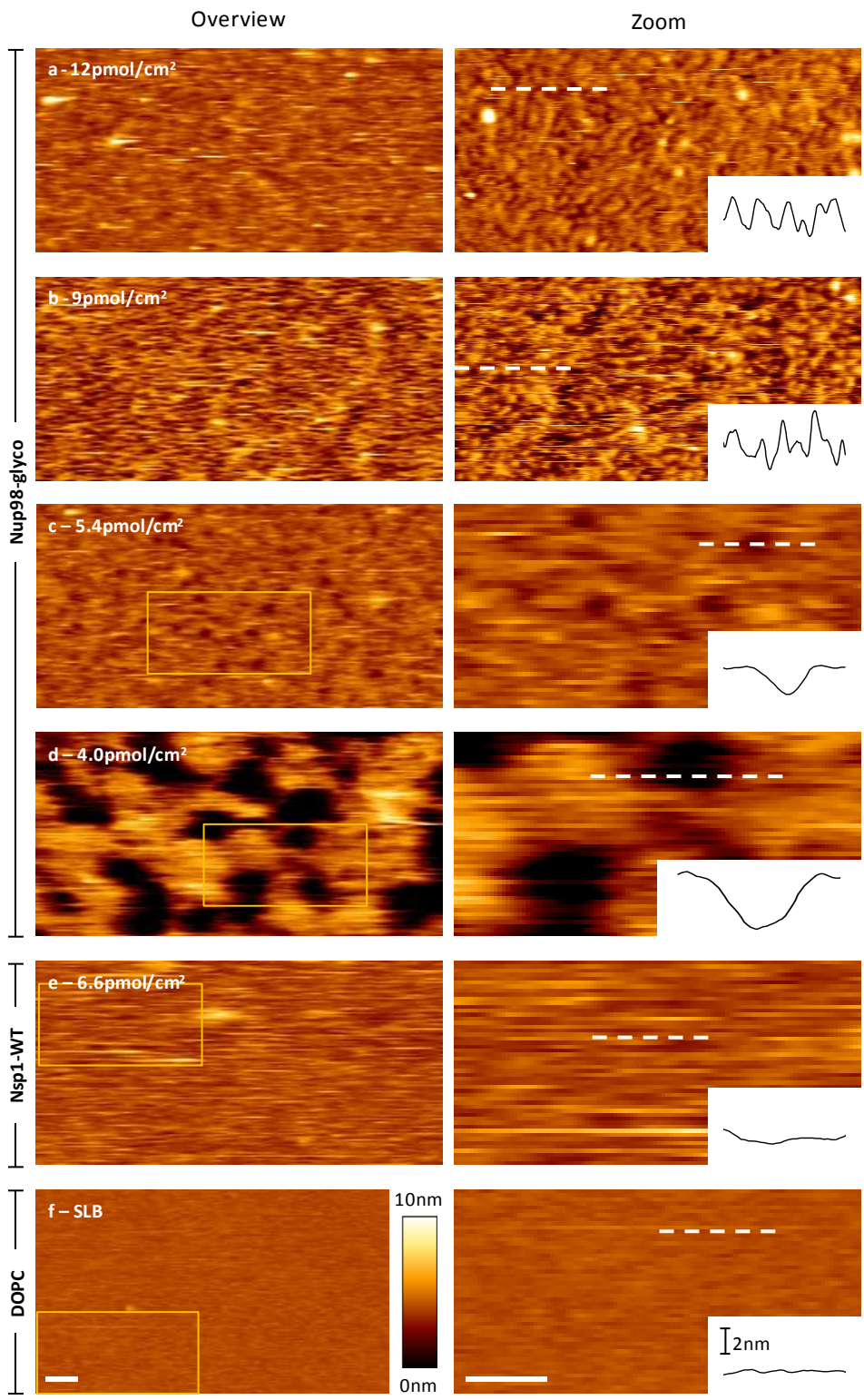

FIGURE 5: Grafting density and cohesive interactions influence the morphology of FG domain assemblies. Images by AFM of different FG repeat domain films. The left column shows low magnification images ($2.5 \times 1.25\ \mu m^2$). The right column shows images at higher

magnification ($1 \times 0.5\ \mu m^2$), which were either obtained by digital zoom (from zones encased by orange solid lines in the left column) or by imaging at a higher resolution. Nup98-glyco films at a grafting density of (*a*) 12 and (*b*) 9 pmol/cm^2 show a homogeneous surface with a distinct and stable small-scale morphology. (*c*) At 5.4 pmol/cm^2 shallow depressions of typically 100 nm width and a few nm in depth appear. (*d*) At 4.0 pmol/cm^2 the film becomes highly heterogeneous, with holes of several 100 nm in width that are likely to fully traverse the film. (*e*) Nsp1-WT films at 6.6 pmol/cm^2 appear homogeneous with some apparent roughness that could not be imaged stably. (*f*) Control image of a pure SLB. Color bar: false color coding of relative heights; scale bars: 200 nm; insets show height profiles of selected scan lines (*white dashed lines*).

We believe that these holes traverse the film completely, even though the apparent depth of the holes in Fig. 5 *d* (approximately 5 nm) is likely to be smaller than the unperturbed thickness of the surrounding film. Most likely, the discrepancy arises because the FG domain film is transiently compressed upon encounter with the AFM probe, even under the gentlest imaging conditions. Indeed, we observed the measured depth of the holes to sensitively depend on the imaging conditions, i.e. a subtle decrease in the AFM cantilever's setpoint amplitude, which is a measure of the pressure that the AFM probe exerts on the film, entailed a significant further reduction (by a few nm) in apparent depth (data not shown).

Despite the films' compliance, the lateral surface features of all Nup98-glyco films varied only little, if at all, upon repeated imaging for extended times (up to one hour). Measurements by fluorescence recovery after photobleaching (FRAP; Fig. 6 *a*) confirmed that Nup98-glyco domains have no detectable lateral mobility, despite being anchored to laterally mobile NTA-lipids in a fluid-phase SLB. The stability of film morphology is direct evidence that inter-chain interactions within end-grafted Nup98-glyco assemblies are sufficiently strong to drive self-organization into temporally stable (i.e. non-fluid) and rather dense hydrogel phases at the nm scale. If the grafting density is too low, the hydrogel phase is disrupted. In contrast, if the density is sufficiently high, a laterally homogeneous hydrogel can form.

Nsp1-WT films, formed at 6.6 pmol/cm^2, were laterally homogeneous but exhibited some apparent roughness (Fig. 5 *e*). In contrast to Nup98-glyco, the surface features varied strongly upon repeated imaging, indicating that the grafted Nsp1-WT molecules retain sufficient mobility to reorganize rapidly. Images of Nsp1-WT and Nsp1-FILV→S films at 5.5 pmol/cm^2 appeared so smooth that they were indistinguishable from images of a pure SLB (Fig. 5 *f*), i.e. they were too soft to be imaged and readily penetrated by the AFM tip. Complementary FRAP measurements provided direct evidence that lateral mobility is retained for Nsp1-WT and Nsp1-FILV→S (Fig. 6 *b*-*c*). Clearly, the cohesive interactions in Nsp1-WT monolayers are too weak to drive the formation of stable aggregates. This result is in contrast with the observation of stable Nsp1-WT hydrogels at the macroscopic level (17,18).

Energy of film compaction

Cohesive interactions effectively lower the free energy of grafted FG domain chains. For $\chi \leq 0.5$, i.e. overall repulsive or weakly cohesive interactions, mean field theory (46) predicts a free energy increase (in units of thermal energy k_BT) of $E \approx 2h^2/(Na^2)$ upon confinement of a chain in the brush, where a is the statistical (Kuhn) segment length (a = 0.76 nm, i.e. twice the contour length of an amino acid in polypeptides) and N is the number of segments (or half the number of amino acids) per chain. The AFM results for h (Fig. 3 *b*) correspond to free energies of 14 ± 5, 8 ± 5 and $4 \pm 2\ k_BT$, respectively, for Nsp1-FILV→S, Nsp1-WT and Nup98-glyco.

The value for Nup98-glyco should be considered an upper bound, because this FG domain forms only a weak brush, i.e. at the borderline to a disrupted film, under the employed surface coverage (Fig. 5 *c*).

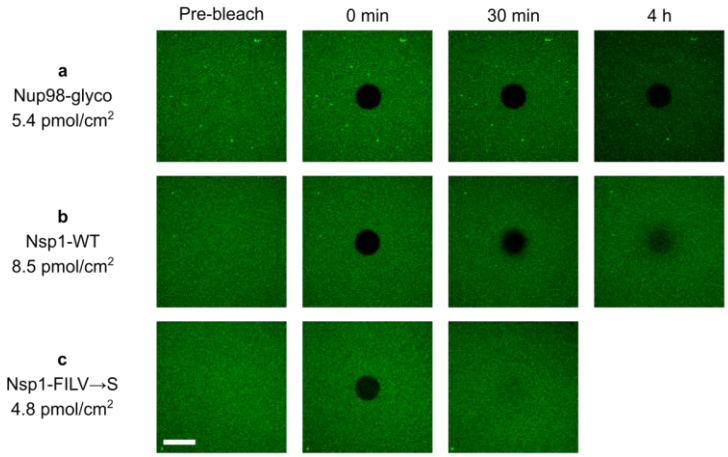

FIGURE 6: Lateral mobility of FG domain films. Measurements by fluorescence recovery after photobleaching (FRAP). (*a*) Nup98-glyco, even at a relatively low surface coverage (5.4 pmol/cm^2), did not show any significant recovery of the bleached central spot within 4 h. (*b*) In contrast, a slow yet significant recovery was observed for Nsp1-WT even at close-to-maximal surface density, demonstrating that the FG domains are laterally mobile within the film. (*c*) Also Nsp1-FILV→S showed recovery, which was quicker and almost complete within 30 min. Scale bar: 30 µm.

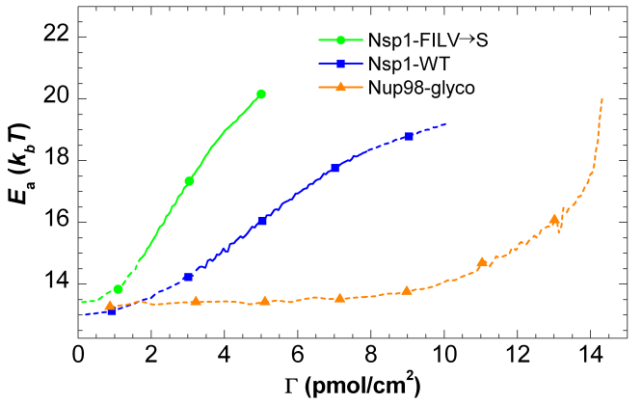

FIGURE 7: Quantification of the energy for FG domain film compaction from binding rates. Activation energies E_a were determined from the FG domain binding rates dΓ/dt in Fig. 2 as a function of grafting density Γ through dΓ/d$t = cA\exp(E_a/k_BT)$, where c = 0.9 µM is the concentration of FG domains in the bulk solution. Following the theoretical considerations for the formation of brushes by Ligoure and Leibler (43), we set $A = 6\pi^2/2^{1/3}\times k_BTM_w/\left(\eta_0 N_A \rho_P a^5 N^2\right) \approx 4.13\,\mathrm{mol\,m\,s^{-1}\,g^{-1}}\times M_w/N^2$. η_0 = 0.9 mPa s is the solution viscosity, N_A = 6.02 × 10^{-23} mol^{-1} is Avogadro's number, ρ_P = 1.36 g/cm^3 is the protein partial specific volume (64), a = 0.76 nm is the statistical (Kuhn) segment length (or twice the contour length of an amino acid), N is the number of segments (or half the number of amino acids) per FG domain chain, and M_w the FG domain molecular weight. As long as binding is

limited by the permeation of an incoming molecule through the FG domain film (*solid lines*), the activation energy is equivalent to the free energy increase associated with partitioning into and stretching of the chain in the film. In the limits of low and high coverage (*dashed lines*), mass transport limitations and saturation of the Ni^{2+}-NTA binding sites on the SLB, respectively, impose an upper limit on the experimentally accessible activation energies. The differences between the activation energies for Nsp1-FILV→S on one hand, and Nsp1-WT or Nup98-glyco on the other, correspond to the energies of film compaction due to cohesive interactions. At 5 pmol/cm^2, it amounts to 3 k_BT for Nsp1-WT and ≥ 7 k_BT for Nup98-glyco.

Provided that binding is limited by the FG domain film, the free energy gains can also be related to binding rates (Fig. 2 *a*) through Arrhenius' law, $d\Gamma/dt = cA \exp(E_a/k_BT)$ (43), where c is the FG domain concentration in the bulk solution and E_a is the activation energy for binding (Fig. 2 *b*). The pre-factor A depends only weakly on the FG domain type, and from the differences in E_a, we estimate energy gains of 3 and 7 k_BT for Nsp1-WT and Nup98-glyco, respectively, compared to Nsp1-FILV→S, at $\Gamma = 5$ pmol/cm^2 (Fig. 7). The value for Nup98-glyco is a lower limit, because binding of this FG domain remained mass transport limited until higher grafting densities. Both approaches for the estimation of energy gains produce similar results. They reveal that the average free energy cost per amino acid, or per FG unit of typically 15 to 20 amino acids, for film compaction is rather small, typically on the order of 0.01, or 0.1 k_BT, respectively.

DISCUSSION

We have used monolayers of selected types of FG domains to study the effect of cohesive interactions on the morphology of FG domain assemblies at the nanoscale. The monolayers mimic the conditions in the native NPC as FG domains are end-grafted to a surface at comparable densities. Under these conditions, cohesive interactions drastically affected various film properties, i.e. formation kinetics, morphology (thickness and lateral homogeneity), chain mobility and mechanical properties. Importantly, the observed morphologies, and their dependence on cohesiveness, are in good qualitative agreement with theoretical predictions for regular, flexible polymer chains as a function of the Flory interaction parameter χ (Fig. 1 *b*). Our study provides evidence that theoretical concepts for regular, flexible polymers are pertinent to predict the self-organization behavior of FG domains. We propose that such concepts are useful to better understand the permeability barrier's mechanism of function.

Impact of cohesive interactions on the morphology and implications for the size selectivity of the permeability barrier

Applying these theoretical concepts to the topology of the NPC transport channel – a cylinder that is short, i.e. the diameter roughly equals the length – and considering that the grafting density in our planar systems is comparable to that in the native NPC, different morphologies would be expected as a function of cohesiveness between polymer chains (Fig. 8). Without cohesive interactions, a continuous polymer meshwork would occupy the entire channel and pervade a rather large space around the channel entrances (Fig. 8 *a*). Balanced inter-chain interactions induce compaction into a denser meshwork (Fig. 8 *b*). If the cohesive interactions become too strong, i.e. at free energy gains well beyond a few k_BT per chain, the continuity of the meshwork is disrupted. Polymer chains may form a collapsed phase near the wall (Fig. 8 *c*), or become partially stretched close to the wall and collapsed at the channel's center (31,47,48).

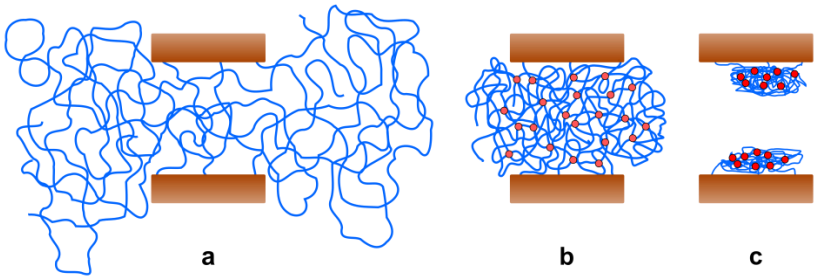

FIGURE 8: Impact of cohesive interactions on the supramolecular FG domain assembly in the NPC topology. Scheme of a cross section along the channel axes, based on predictions from polymer theory for flexible, grafted polymers. (*a*) If the inter-chain interactions are only weakly attractive or repulsive, an extended brush forms, and chains entangle into a meshwork with a characteristic mesh size. (*b*) With moderate inter-FG-domain interactions, the meshwork becomes denser; the characteristic mesh size and the size-exclusion limit decrease. (*c*) Strong cohesive interactions generate a discontinuous and leaky meshwork that fails to fill the entire channel. Tuning the cohesiveness of FG domains hence provides a robust strategy to optimize the size-selectivity of the nuclear pore permeability barrier.

The performance of these morphologies as permeability barriers would differ drastically. Size selectivity would be almost completely lost in the scenario shown in Fig. 8 *c*, because even rather large molecules can rapidly diffuse through spaces that are not occupied by the FG domain meshwork. The assemblies sketched in Figs. 8 *a*-*b* should both feature size-selective permeability, albeit to a different extent (27,33,34). To a first approximation, both assemblies can be characterized by an average mesh size. Molecules smaller than the mesh can readily permeate the FG domain assembly, whereas the diffusion of larger molecules is slowed down (33,34). In meshworks of flexible polymers, the mesh size is predicted to decrease with polymer concentration with a power between 3/4 and 1, depending on χ (33,34,35). Consequently, the roughly two-fold increase in FG domain concentration that we observed between the least cohesive Nsp1-FILV→S and the most cohesive Nup98-glyco (at identical grafting density) would translate into a decrease in the mesh size by 40% or more. This simple estimate illustrates that a compaction of the FG domain meshwork through inter-chain interactions (Fig. 8 *b*) can decrease the size-exclusion limit for inert proteins considerably. We would like to stress that the improvement in size selectivity through film compaction is expected to persist even if the individual inter-chain interactions (or cross-links) are very short lived. In such a "compacted meshwork", the size-exclusion limit arises predominantly from the mutual confinement of interpenetrating polymer chains (33,34). With increasing stability, cross-links add another quality to the meshwork, i.e. they improve size selectivity further, because they enhance the spatial confinement of chains and thereby stabilize the meshes (33). Reconstituted NPCs have so far only been observed to be functional with strongly cohesive FG domains such as Nup98-glyco (21). The relative contribution of compaction and stable cross-links, as formed in a hydrogel, to the size-selective permeability of NPCs, however, remains to be elucidated.

Based on our experimental results and polymer theory concepts, we conjecture that the formation of a dense and continuous pore-filling phase of FG domains is a viable strategy to create a barrier that effectively excludes inert molecules based on their size. Tuning of the overall cohesiveness emerges as a robust and efficient way to generate such architecture for the grafting densities and FG domain contour lengths that are typical in NPCs. At the same time,

such a phase would enable translocation of NTRs, according to the selective phase model, as previously demonstrated *in vitro* with macroscopic FG domain hydrogels (18,25,49) and reconstituted NPCs (21). In the presence of NTRs, FG domain meshworks were found to have enhanced size selectivity (28,50). Further studies on FG domain monolayers should aim at understanding how NTRs affect the morphology (26,51), size selectivity, and mechanical properties (27) of FG domain meshworks.

FG domains can form nanoscopic hydrogels

Structural characterization by AFM (Fig. 5 *a*-*c*) and FRAP analysis (Fig. 6 *a*) provides strong evidence that, in physiological buffer, end-grafted Nup98-gyco assembles into a non-fluid, water-retaining phase, i.e. a hydrogel. This implies that FG domains can retain hydrogel properties even in assemblies with dimensions comparable to the NPC, where the size of the assembly is only a few times larger than the native extension of the individual molecules in isolation. From a comparison of the phase behavior of irregular FG domains (Fig. 5 *a*-*c*) with theoretical predictions for regular polymers (Fig. 1 *b*), we conclude that the "effective" Flory interaction parameter $\bar{\chi}$ for Nup98-glyco must be above 0.5.

The Nsp1-WT FG domain forms stable macroscopic hydrogels (17), and also, in the end-grafted nanoscopic system, interactions were clearly evident by the more rapid assembly (Fig. 2), decreased thickness (Fig. 3) and increased stiffness (Fig. 4) of the Nsp1-WT film as compared to the FILV→S mutant. Nevertheless, Nsp1-WT films remained softer and more mobile than Nup98-glyco films (Figs. 4-6), perhaps because only the N-terminal part (residues 1 to 175) of the Nsp1 FG domain is more cohesive than the C-terminal part (residues ~200 to 600). A selective permeability barrier in FG-domain-depleted NPCs could be restored by Nup98-glyco or by a multiplied N-terminal part of the Nsp1 FG domain, but not by the complete Nsp1p-WT domain (21), although also the latter forms highly selective macroscopic hydrogels (17,18,21,25). This suggests that nanoscopic „details" might be of critical functional significance. Indeed, it appears possible that an end-grafted Nsp1-WT domain forms a layered architecture with a gel-like layer originating from its more cohesive portion and a more liquid (and more permeable) layer that originates from its larger less cohesive part and allows non-selective fluxes of macromolecules through the NPC. Since Nsp1-WT does not form disrupted films, we conclude that $\bar{\chi}$ must be around or less than 0.5.

Impact of cohesive interactions on NPC biogenesis and stability

Fig. 2 demonstrates that cohesive interactions can greatly facilitate the assembly of end-grafted FG domain meshworks. Because the NPC is a self-assembled architecture, this effect might be important for the rate of NPC biogenesis. Moreover, stretching of grafted chains in a brush at NPC-relevant grafting densities entails entropic penalties that can readily amount to 10 $k_{\mathrm{B}}T$ or more. Unless equilibrated by cohesive inter-chain interactions, this penalty decreases the stability of FG domain anchorage. We therefore propose that cohesive interactions facilitate (and might even be essential for) the correct and timely assembly and for the stability of the permeability barrier. Indeed, a Nup98-FIL→S mutant, were F, I and L residues were mutated to serines to minimize cohesive interactions, was found to require higher concentrations for efficient incorporation into reconstituted NPCs than wild type Nup98-glyco (21).

Impact of heterogeneities on the performance of the permeability barrier

We argued above that a continuous pore-filling meshwork is required for the correct function of the permeability barrier. This meshwork, however, may not be entirely homogeneous. For example, it is well known that the density of non-cohesive polymers in planar brushes exhibits a

parabolic profile in the direction normal to the surface (52,53). Spatial variations in the FG repeat density might very well occur inside the NPC, both along and perpendicular to the channel axis, owing to the geometrical constraints of the channel (48,54). Variations in FG repeat density and cohesiveness within (19,32) and between (20) individual FG domains might contribute further heterogeneities, as illustrated by a recent simulation study (54).

In particular, such variations could explain the results by Ma et al. (55) who proposed preferred transport paths for inert molecules and NTRs, respectively, that were spatially separated yet interdependent. Recent simulations by Osmanovic et al. (47) suggest that tuning of cohesiveness sensibly affects the distribution of FG repeats perpendicular to the channel axis. We conclude that the results by Ma et al. do not represent firm evidence against the selective phase model, as had been proposed by the authors. Instead, we conjecture that the location of transport paths may vary between cellular species as a function of the fine tuning of cohesive interactions, but that the existence of a preferred path at a precise location is not essential for the functionality of the permeability barrier.

Cohesiveness of FG domains and the position of FG domains in the NPC might also be interconnected to further optimize size and species selectivity of the permeability barrier. For example, FG domains that are located at the periphery of the permeability barrier might be less cohesive, to occupy a larger volume for catching NTRs from solution, while FG domains in the center could show stronger cohesion to form a tight and highly size-selective meshwork (20).

Clearly, such heterogeneity effects cannot be captured by simple theories of flexible polymers. Their understanding is likely to require more sophisticated theoretical (47,56) and experimental approaches that consider explicitly the heterogeneous primary structure of FG domains and/or the topology of NPCs. We have therefore intentionally chosen to keep our comparison between theory and experiment largely on a qualitative level. However, we propose that the simple conceptual approach presented here captures essential features underlying the function of the permeability barrier.

CONCLUSION

To summarize, we have demonstrated that FG domain monolayers show different film formation kinetics, morphologies, dynamics, and mechanical properties depending on the type of employed FG domain. In agreement with predictions from polymer theory we attribute these findings to different degrees of cohesive interactions between FG domains. Based on the analysis of our data in terms of simple theoretical concepts for assemblies of flexible polymers with varying Flory interaction parameter χ, we propose the formation of a compact FG domain assembly that fills the entire pore – a compacted meshwork – as a key design principle for a functional permeability barrier. Tuning of inter-chain interactions, within the range of a few $k_{\mathrm{B}}T$ of free energy per chain, emerges as a robust and effective tool to optimize functionality. It should be beneficial for the biogenesis and stability of NPCs, and useful as a design rule for the engineering of man-made species-selective filtering devices.

ACKNOWLEDGEMENTS

We thank Jacob Piehler (Osnabrück, Germany) for providing NTA-functionalized lipids, and Oleg Borisov (Pau, France) for fruitful discussions. R.P.R. acknowledges funding from the Spanish Ministry of Science and Innovation (MICINN, refs RYC2009-04275 and MAT2011-24306), the European Research Council (Starting Grant 306435) and the Department of Industry

of the Basque Government. N.B.E. was supported by the Göttingen Graduate School for Neuroscience, Biophysics and Molecular Biosciences (DFG Grant GSC 226/1).

SUPPORTING CITATIONS

References (57,58,59,60,61,62,63) appear in the Supporting Material.

REFERENCES

1. Görlich, D. and U. Kutay. 1999. Transport between the cell nucleus and the cytoplasm. Annu Rev Cell Dev Biol 15:607-660.
2. Macara, I. G. 2001. Transport into and out of the nucleus. Microbiol Mol Biol Rev 65:570-594.
3. Fried, H. and U. Kutay. 2003. Nucleocytoplasmic transport: taking an inventory. Cell Mol Life Sci 60:1659-1688.
4. Walde, S. and R. H. Kehlenbach. 2010. The Part and the Whole: functions of nucleoporins in nucleocytoplasmic transport. Trends Cell Biol 20:461-469.
5. Fernandez-Martinez, J. and M. P. Rout. 2012. A jumbo problem: mapping the structure and functions of the nuclear pore complex. Curr Opin Cell Biol 24:92-99.
6. Grossman, E., O. Medalia, and M. Zwerger. 2012. Functional architecture of the nuclear pore complex. Annu Rev Biophys 41:557-584.
7. Yang, Q., M. P. Rout, and C. W. Akey. 1998. Three-dimensional architecture of the isolated yeast nuclear pore complex: functional and evolutionary implications. Molecular Cell 1:223-234.
8. Maimon, T., N. Elad, I. Dahan, and O. Medalia. 2012. The human nuclear pore complex as revealed by cryo-electron tomography. Structure 20:998-1006.
9. Strawn, L. A., T. Shen, N. Shulga, D. S. Goldfarb, and S. R. Wente. 2004. Minimal nuclear pore complexes define FG repeat domains essential for transport. Nat Cell Biol 6:197-206.
10. Mohr, D., S. Frey, T. Fischer, T. Güttler, and D. Görlich. 2009. Characterisation of the passive permeability barrier of nuclear pore complexes. EMBO J 28:2541-2553.
11. Cook, A., F. Bono, M. Jinek, and E. Conti. 2007. Structural biology of nucleocytoplasmic transport. Annu Rev Biochem 76:647-671.
12. Ribbeck, K. and D. Görlich. 2001. Kinetic analysis of translocation through nuclear pore complexes. EMBO J 20:1320-1330.
13. Ribbeck, K. and D. Görlich. 2002. The permeability barrier of nuclear pore complexes appears to operate via hydrophobic exclusion. EMBO J 21:2664-2671.
14. Rout, M. P., J. D. Aitchison, M. O. Magnasco, and B. T. Chait. 2003. Virtual gating and nuclear transport: the hole picture. Trends Cell Biol 13:622-628.
15. Peters, R. 2005. Translocation through the nuclear pore complex: selectivity and speed by reduction-of-dimensionality. Traffic 6:421-427.
16. Lim, R. Y., B. Fahrenkrog, J. Koser, K. Schwarz-Herion, J. Deng, and U. Aebi. 2007. Nanomechanical basis of selective gating by the nuclear pore complex. Science 318:640-643.
17. Frey, S., R. P. Richter, and D. Görlich. 2006. FG-rich repeats of nuclear pore proteins form a three-dimensional meshwork with hydrogel-like properties. Science 314:815-817.
18. Frey, S. and D. Görlich. 2007. A saturated FG-repeat hydrogel can reproduce the permeability properties of nuclear pore complexes. Cell 130:512-523.

19. Ader, C., S. Frey, W. Maas, H. B. Schmidt, D. Görlich, and M. Baldus. 2010. Amyloid-like interactions within nucleoporin FG hydrogels. Proc Natl Acad Sci U S A 107:6281-6285.
20. Patel, S. S., B. J. Belmont, J. M. Sante, and M. F. Rexach. 2007. Natively unfolded nucleoporins gate protein diffusion across the nuclear pore complex. Cell 129:83-96.
21. Hülsmann, B. B., A. A. Labokha, and D. Görlich. 2012. The permeability of reconstituted nuclear pores provides direct evidence for the selective phase model. Cell 150:738-751.
22. Denning, D. P., S. S. Patel, V. Uversky, A. L. Fink, and M. Rexach. 2003. Disorder in the nuclear pore complex: the FG repeat regions of nucleoporins are natively unfolded. Proc Natl Acad Sci U S A 100:2450-2455.
23. Denning, D. P. and M. F. Rexach. 2007. Rapid evolution exposes the boundaries of domain structure and function in natively unfolded FG nucleoporins. Mol Cell Proteomics 6:272-282.
24. Rout, M. P. and S. R. Wente. 1994. Pores for thought: nuclear pore complex proteins. Trends Cell Biol 4:357-365.
25. Labokha, A. A., S. Gradmann, S. Frey, B. B. Hülsmann, H. Urlaub, M. Baldus, and D. Görlich. 2012. Systematic analysis of barrier-forming FG hydrogels from *Xenopus* nuclear pore complexes. EMBO J. 32:204-218.
26. Eisele, N. B., S. Frey, J. Piehler, D. Görlich, and R. P. Richter. 2010. Ultrathin nucleoporin phenylalanine-glycine repeat films and their interaction with nuclear transport receptors. EMBO Rep 11:366-372.
27. Eisele, N. B., F. I. Andersson, S. Frey, and R. P. Richter. 2012. Viscoelasticity of thin biomolecular films: a case study on nucleoporin phenylalanine-glycine repeats grafted to a histidine-tag capturing QCM-D sensor. Biomacromolecules 13:2322-2332.
28. Jovanovic-Talisman, T., J. Tetenbaum-Novatt, A. S. McKenney, A. Zilman, R. Peters, M. P. Rout, and B. T. Chait. 2009. Artificial nanopores that mimic the transport selectivity of the nuclear pore complex. Nature 457:1023-1027.
29. Borisov, O. V., Y. B. Zhulina, and T. M. Birshtein. 1988. Constitutional diagram and collapse of grafted chain layers. Polymer Sci U S S R 30:772-779.
30. Zhulina, E. B., T. M. Birshtein, V. A. Priamitsyn, and L. I. Klushin. 1995. Inhomogeneous structure of collapsed polymer brushes under deformation. Macromolecules 28:8612-8620.
31. Tagliazucchi, M. and I. Szleifer. 2012. Stimuli-responsive polymers grafted to nanopores and other nano-curved surfaces: structure, chemical equilibrium and transport. Soft Matter 8:7292-7305.
32. Yamada, J., J. L. Phillips, S. Patel, G. Goldfien, A. Calestagne-Morelli, H. Huang, R. Reza, J. Acheson, V. V. Krishnan, S. Newsam, A. Gopinathan, E. Y. Lau, M. E. Colvin, V. N. Uversky, and M. F. Rexach. 2010. A bimodal distribution of two distinct categories of intrinsically disordered structures with separate functions in FG nucleoporins. Mol Cell Proteomics 9:2205-2224.
33. Rubinstein, M. and R. H. Colby. 2003. Polymer Physics. Oxford: Oxford University Press.
34. Cai, L. H., S. Panyukov, and M. Rubinstein. 2011. Mobility of spherical probe objects in polymer liquids. Macromolecules 44:7853-7863.
35. de Gennes, P.-G. 1979. Scaling Concepts in Polymer Physics: Cornel University Press.
36. Jones, R. G., E. S. Wilks, W. V. Metanomski, J. Kahovec, M. Hess, R. Stepto, and T. Kitayama, editors. 2009. Compendium of Polymer Terminology and Nomenclature, IUPAC Recommendations 2008: RSC. 464 p.

37. Peters, R. 2009. Translocation through the nuclear pore: Kaps pave the way. Bioessays 31:466-477.
38. Lata, S., M. Gavutis, and J. Piehler. 2006. Monitoring the dynamics of ligand-receptor complexes on model membranes. J Am Chem Soc 128:6-7.
39. Lata, S., A. Reichel, R. Brock, R. Tampé, and J. Piehler. 2005. High-affinity adaptors for switchable recognition of histidine-tagged proteins. J Am Chem Soc 127:10205-10215.
40. Reviakine, I., D. Johannsmann, and R. P. Richter. 2011. Hearing what you cannot see and visualizing what you hear: interpreting quartz crystal microbalance data from solvated interfaces. Anal Chem 83:8838-8848.
41. Carton, I., A. R. Brisson, and R. P. Richter. 2010. Label-free detection of clustering of membrane-bound proteins. Anal Chem 82:9275-9281.
42. De Feijter, J. A., J. Benjamins, and F. A. Veer. 1978. Ellipsometry as a tool to study the adsorption behavior of synthetic and biopolymers at the air-water interface. Biopolymers 17:1759-1772.
43. Ligoure, C. and L. Leibler. 1990. Thermodynamics and kinetics of grafting end-functionalized polymers to an interface. J Phys France 51:1313-1328.
44. Rout, M. P., J. D. Aitchison, A. Suprapto, K. Hjertaas, Y. Zhao, and B. T. Chait. 2000. The yeast nuclear pore complex: composition, architecture, and transport mechanism. J Cell Biol 148:635-651.
45. Du, B. and D. Johannsmann. 2004. Operation of the quartz crystal microbalance in liquids: derivation of the elastic compliance of a film from the ratio of bandwidth shift and frequency shift. Langmuir 20:2809-2812.
46. Zhulina, E. B., O. V. Borisov, and V. A. Priamitsyn. 1990. Theory of steric stabilization of colloid dispersions by grafted polymers. J Colloid Interface Sci 137:495-511.
47. Osmanovic, D., J. Bailey, A. H. Harker, A. Fassati, B. W. Hoogenboom, and I. J. Ford. 2012. Bistable collective behavior of polymers tethered in a nanopore. Phys Rev E 85:061917.
48. Peleg, O., M. Tagliazucchi, M. Kroger, Y. Rabin, and I. Szleifer. 2011. Morphology control of hairy nanopores. ACS nano 5:4737-4747.
49. Milles, S. and E. A. Lemke. 2011. Single molecule study of the intrinsically disordered FG-repeat nucleoporin 153. Biophys J 101:1710-1719.
50. Frey, S. and D. Görlich. 2009. FG/FxFG as well as GLFG repeats form a selective permeability barrier with self-healing properties. EMBO J 28:2554-2567.
51. Schoch, R. L., L. E. Kapinos, and R. Y. Lim. 2012. Nuclear transport receptor binding avidity triggers a self-healing collapse transition in FG-nucleoporin molecular brushes. Proc Natl Acad Sci U S A 109:16911-16916.
52. Milner, S. T. 1991. Polymer brushes. Science 251:905-914.
53. Zhulina, E. B., V. A. Priamitsyn, and O. V. Borisov. 1989. Structure and conformational transitions in grafted polymer chain layers. A new theory. Polymer Sci U S S R 31:205-216.
54. Tagliazucchi, M., O. Peleg, M. Kroger, Y. Rabin, and I. Szleifer. 2013. Effect of charge, hydrophobicity, and sequence of nucleoporins on the translocation of model particles through the nuclear pore complex. Proc Natl Acad Sci U S A.
55. Ma, J., A. Goryaynov, A. Sarma, and W. Yang. 2012. Self-regulated viscous channel in the nuclear pore complex. Proc Natl Acad Sci U S A 109:7326-7331.

56. Mincer, J. S. and S. M. Simon. 2011. Simulations of nuclear pore transport yield mechanistic insights and quantitative predictions. Proc Natl Acad Sci U S A 108:E351-358.
57. Hermens, W. T., M. Beneš, R. Richter, and H. Speijer. 2004. Effects of flow on solute exchange between fluids and supported biosurfaces. Biotechn Appl Biochem 39:277-284.
58. Bingen, P., G. Wang, N. F. Steinmetz, M. Rodahl, and R. P. Richter. 2008. Solvation effects in the QCM-D response to biomolecular adsorption - a phenomenological approach. Anal Chem 80:8880-8890.
59. Kohn, J. E., I. S. Millett, J. Jacob, B. Zagrovic, T. M. Dillon, N. Cingel, R. S. Dothager, S. Seifert, P. Thiyagarajan, T. R. Sosnick, M. Z. Hasan, V. S. Pande, I. Ruczinski, S. Doniach, and K. W. Plaxco. 2004. Random-coil behavior and the dimensions of chemically unfolded proteins. Proc Natl Acad Sci U S A 101:12491-12496.
60. Tcherkasskaya, O., E. A. Davidson, and V. N. Uversky. 2003. Biophysical constraints for protein structure prediction. J Proteome Res 2:37-42.
61. Richter, R. P., R. Bérat, and A. R. Brisson. 2006. The formation of solid-supported lipid bilayers - an integrated view. Langmuir 22:3497-3505.
62. Domack, A., O. Prucker, J. Rühe, and D. Johannsmann. 1997. Swelling of a polymer brush probed with a quartz crystal resonator. Phys Rev E 56:680-689.
63. Johannsmann, D. http://www2.pc.tu-clausthal.de/dj/software_en.shtml.
64. Zhao, H., P. H. Brown, and P. Schuck. 2011. On the distribution of protein refractive index increments. Biophys J 100:2309-2317.

SUPPORTING MATERIAL

Cohesiveness tunes assembly and morphology of FG nucleoporin domain meshworks – Implications for nuclear pore permeability

Nico B. Eisele[†‡], *Aksana A. Labokha*[‡], *Steffen Frey*[‡], *Dirk Görlich*[‡], *Ralf P. Richter*[†§¶*]

[†] Biosurfaces Unit, CIC biomaGUNE, Paseo Miramon 182, 20009 San Sebastian, Spain

[‡] Department of Cellular Logistics, Max Planck Institute for Biophysical Chemistry, Am Faßberg 11, 37077 Göttingen, Germany

[§] I2BM, Department of Molecular Chemistry, J. Fourier University, 570 Rue de la Chimie, 38041 Grenoble Cedex 9, France

[¶] Max Planck Institute for Intelligent Systems, Heisenbergstraße 3, 70569 Stuttgart, Germany

* Correspondence: rrichter@cicbiomagune.es

SUPPORTING METHODS

Quantification of mass transport limited FG domain adsorption rates. In our experimental in situ ellipsometry setup, i.e. a flat surface opposite a rotating stirrer, transport of molecules to the film can be adequately described by diffusion through an unstirred layer next to the surface (1). The mass transport limited adsorption rate of FG domains can be estimated from a reference measurement of an adsorption process that is limited by mass transport and that occurs under identical stirring conditions (1):

$$\left(\frac{\partial \Gamma}{\partial t}\right)_{\mathrm{FG}} = \left(\frac{R_{\mathrm{ref}}}{R_{\mathrm{FG}}}\right)^{2/3} \frac{[\mathrm{FG}]}{[\mathrm{ref}]} \left(\frac{\partial \Gamma}{\partial t}\right)_{\mathrm{ref}}.$$

We chose the adsorption of avidin with a concentration of 0.1 μM to a biotinylated SLB (2) as the reference and measured an adsorption rate of $(\partial\Gamma/\partial t)_{\mathrm{ref}} = 2.07 \pm 0.12\,\mathrm{pmol/cm^2/min}$ (mean ± standard deviation from three measurements). The Stokes radius for avidin is $R_{\mathrm{ref}} = 3.4\,\mathrm{nm}$, and we estimate R_{FG} to be between 3.5 and 8.7 nm, based on reported values for other FG domains (3,4) and other intrinsically disordered or chemically denatured proteins (5,6). These considerations lead to a mass transport limited adsorption rate for FG domains between 7.6 and 21.5 pmol/cm^2/min at a bulk concentration of 0.9 ± 0.1 μM. This range is represented as a gray-shaded area in Fig. 2 *a*.

SUPPORTING FIGURES

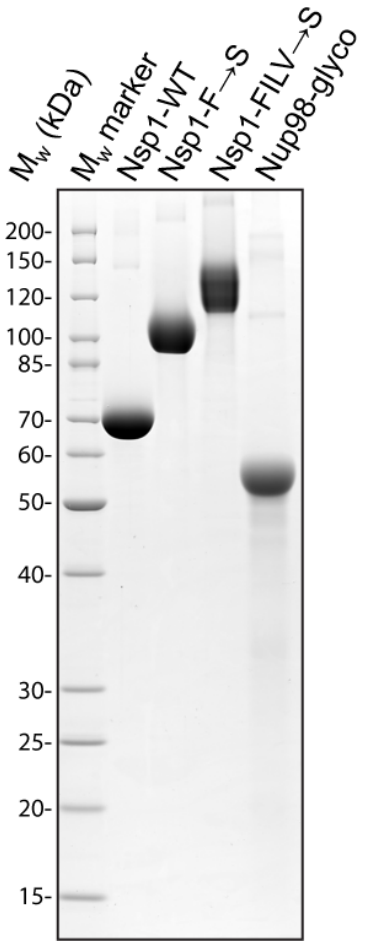

FIGURE S1: Quality of purified recombinant FG domains used in this study. FG domains with His-tag were dissolved in 30% formamide and diluted 1:10 in SDS sample buffer. 2.5 µg of each protein was resolved by SDS-PAGE and stained with Coomassie G250. All preparations contain more than 90% full length protein.

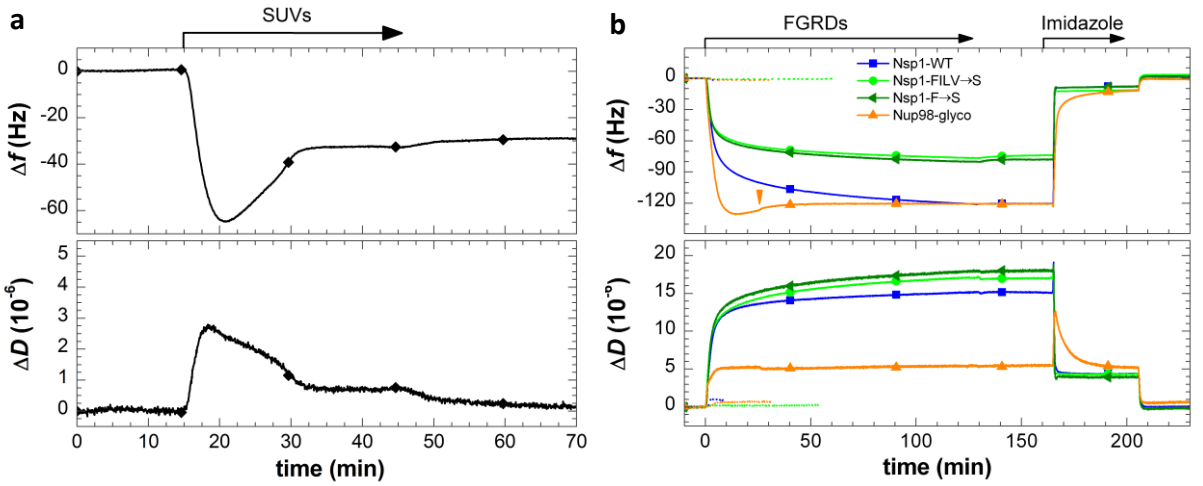

FIGURE S2: FG domains are anchored specifically and stably through their terminal His-tags to NTA-functionalized SLBs. (*a*) SLB formation monitored by QCM-D. Silica surfaces in working buffer were exposed to 50 µg/ml SUVs made of 90 mol-% DOPC and 10 mol-% bis-NTA-functionalized lipids. Start and duration of the incubation is indicated by an arrow. The two-phase behavior together with the final changes in frequency and dissipation of Δf = -28 Hz and $\Delta D < 0.3 \cdot 10^{-6}$, respectively, characterizes the formation of an SLB of good quality (7). The minor shifts in Δf and ΔD at about 44 min are due to the removal of $NiCl_2$ from the solution during rinsing in working buffer. (*b*) Formation of FG domain films was monitored by QCM-D on SLBs formed from SUVs containing either a mixture of 90 mol-% DOPC and 10 mol-% bis-NTA-functionalized lipids (*solid lines*), or only DOPC (*dotted lines*). Baselines (i.e. $\Delta f = \Delta D = 0$) correspond to the responses for bare SLBs. Start and duration of incubation steps with different samples are indicated with solid arrows on top of the plot. After each incubation step, the solution phase was replaced by working buffer. Strong changes in frequency and dissipation upon incubation with different His-tagged FG domain species (*listed in the legend*) at 45 µg/ml (i.e. 0.7 µM Nsp1-FILV→S, Nsp1-F→S and Nsp1-WT and 0.8 µM Nup98-glyco) on NTA-functionalized SLBs reflect the formation of soft and hydrated films. No changes in Δf and ΔD for Nsp1-derived FG domains and minor changes for Nup98-glyco upon rinsing in buffer (rinsing of Nup98-glyco was performed at 25 min, i.e. earlier than for the other species; *orange arrowhead*) indicate stable grafting. After exposure to 500 mM imidazole at pH 7.4, Δf and ΔD return to baseline levels, demonstrating specificity of binding. Changes in Δf and ΔD upon exchange from imidazole containing solution to pure working buffer do not reflect any changes on the surface but result from a change in the viscosity and/or density of the surrounding solution owing to the presence of imidazole. When exposed at 90 µg/ml (i.e. 1.5 µM Nsp1-FILV→S, Nsp1-F→S, and Nup98-glyco and 1.4 µM Nsp1-WT) to SLBs made of pure DOPC, none of the His-tagged FG domains induced appreciable QCM-D responses, confirming that the FG domains do not bind to SLBs that lack NTA functionality.

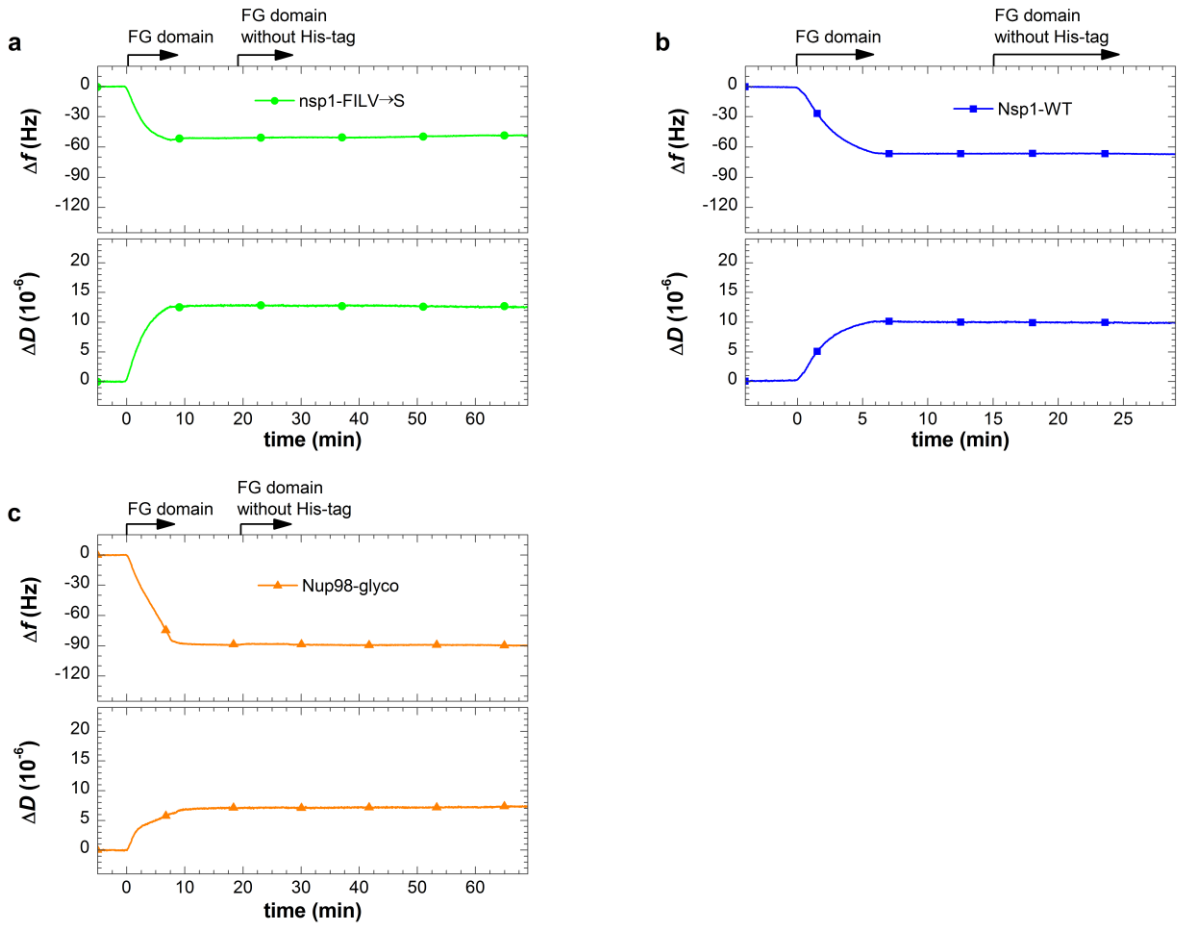

FIGURE S3: All FG domains in the films are anchored to the SLB. SLBs with 10 mol-% bis-NTA functionalized lipids were formed and incubated with His-tagged FG domains at a concentration of 23 µg/ml (0.4 µM). Incubation was interrupted, by rinsing in working buffer, when frequency shifts reached between 50 and 70 % of the maximal frequency shifts observed in Fig. S1 *b*. No changes in Δf and ΔD were observed when the films were subsequently incubated with the same FG domain types lacking the His-tags at identical concentration. We conclude that homophilic interactions or entanglements are not sufficient to entrap individual FG domains stably in the films. All stably bound FG domain molecules must hence be anchored to the SLB.

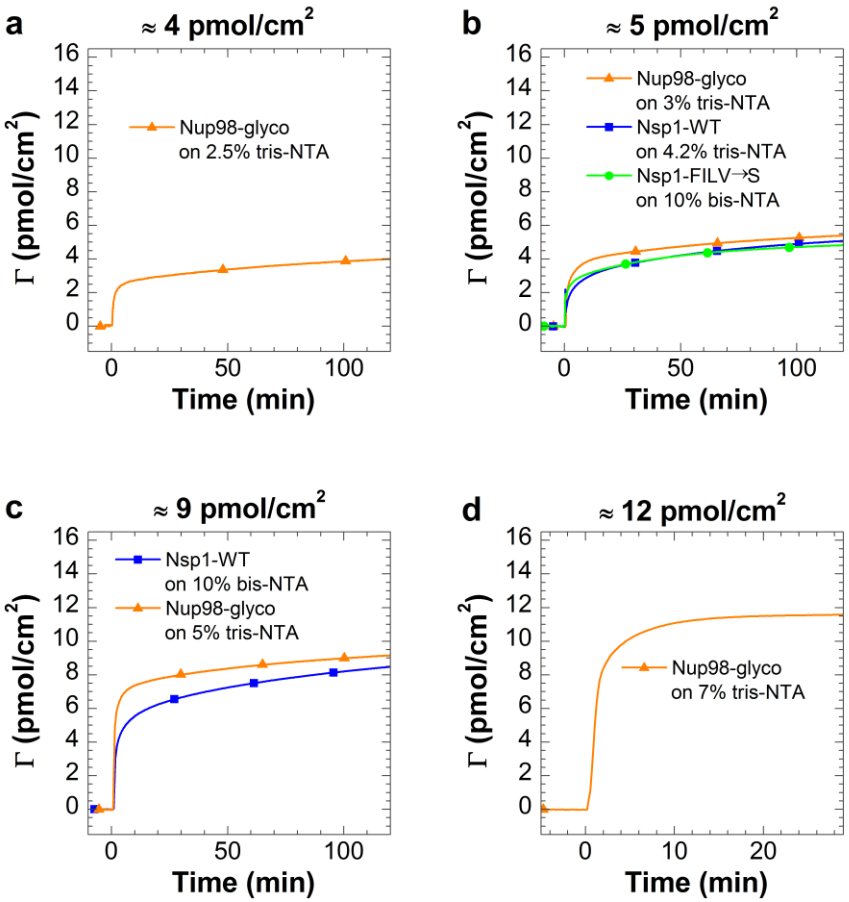

FIGURE S4: Tuning FG domain surface density. FG domain films with defined and reproducible grafting densities (*indicated on top of each plot*) were obtained by tuning the valency (*bis* or *tris*) and fraction (in mol-%) of NTA-functionalized lipids in the SUVs from which the SLBs were formed (*indicated in each plot*). FG domains were incubated at concentrations of 56 μg/ml (1.0 μM) for Nup98-glyco and 113 μg/ml (1.8 μM) for Nsp1-WT and (1.9 μM) Nsp1-FILV→S.

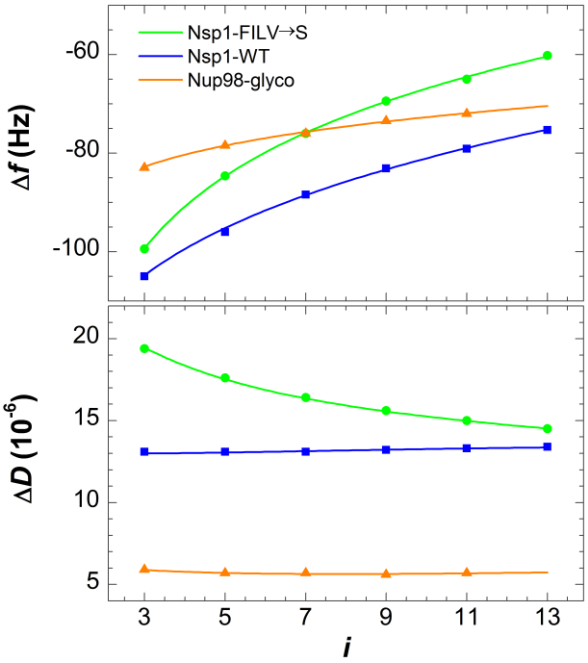

FIGURE S5: FG domain film thickness determination from QCM-D data. Film thickness was estimated by fitting the QCM-D data for all overtones to a continuum viscoelastic model (8) with the software QTM (D. Johannsmann, Technical University of Clausthal, Germany (9); option "small load approximation"), as described in detail elsewhere (10). The model relates the measured QCM-D responses, Δf and ΔD as a function of the overtone number, to the viscoelastic properties and the thickness of the surface-confined film (10,11). The figure shows the final QCM-D responses (*symbols*) for the formation of FG domain films of about 5 pmol/cm^2 (see Fig. S3 *b* for film formation conditions; FG domain type is indicated in the plot) together with the best fits (*lines*) as a function of overtone *i*. Resulting film thicknesses are shown in Fig. 3 *b*, where error bars correspond to joint confidence regions with a confidence level of one standard deviation, and were determined as described in ref. (10).

SUPPORTING REFERENCES

1. Hermens, W. T., M. Beneš, R. Richter, and H. Speijer. 2004. Effects of flow on solute exchange between fluids and supported biosurfaces. Biotechn Appl Biochem 39:277-284.
2. Bingen, P., G. Wang, N. F. Steinmetz, M. Rodahl, and R. P. Richter. 2008. Solvation effects in the QCM-D response to biomolecular adsorption - a phenomenological approach. Anal Chem 80:8880-8890.
3. Denning, D. P., S. S. Patel, V. Uversky, A. L. Fink, and M. Rexach. 2003. Disorder in the nuclear pore complex: the FG repeat regions of nucleoporins are natively unfolded. Proc Natl Acad Sci U S A 100:2450-2455.
4. Yamada, J., J. L. Phillips, S. Patel, G. Goldfien, A. Calestagne-Morelli, H. Huang, R. Reza, J. Acheson, V. V. Krishnan, S. Newsam, A. Gopinathan, E. Y. Lau, M. E. Colvin, V. N. Uversky, and M. F. Rexach. 2010. A bimodal distribution of two distinct categories of intrinsically disordered structures with separate functions in FG nucleoporins. Mol Cell Proteomics 9:2205-2224.
5. Kohn, J. E., I. S. Millett, J. Jacob, B. Zagrovic, T. M. Dillon, N. Cingel, R. S. Dothager, S. Seifert, P. Thiyagarajan, T. R. Sosnick, M. Z. Hasan, V. S. Pande, I. Ruczinski, S. Doniach, and K. W. Plaxco. 2004. Random-coil behavior and the dimensions of chemically unfolded proteins. Proc Natl Acad Sci U S A 101:12491-12496.
6. Tcherkasskaya, O., E. A. Davidson, and V. N. Uversky. 2003. Biophysical constraints for protein structure prediction. J Proteome Res 2:37-42.
7. Richter, R. P., R. Bérat, and A. R. Brisson. 2006. The formation of solid-supported lipid bilayers - an integrated view. Langmuir 22:3497-3505.
8. Domack, A., O. Prucker, J. Rühe, and D. Johannsmann. 1997. Swelling of a polymer brush probed with a quartz crystal resonator. Phys Rev E 56:680-689.
9. Johannsmann, D. http://www2.pc.tu-clausthal.de/dj/software_en.shtml.
10. Eisele, N. B., F. I. Andersson, S. Frey, and R. P. Richter. 2012. Viscoelasticity of thin biomolecular films: a case study on nucleoporin phenylalanine-glycine repeats grafted to a histidine-tag capturing QCM-D sensor. Biomacromolecules 13:2322-2332.
11. Reviakine, I., D. Johannsmann, and R. P. Richter. 2011. Hearing what you cannot see and visualizing what you hear: interpreting quartz crystal microbalance data from solvated interfaces. Anal Chem 83:8838-8848.